Phase separation dynamics of simple liquids in non-uniform electric fields

Jennifer Galanis and Yoav Tsori
Department of Chemical Engineering, Ben-Gurion University of the Negev, Beer-Sheva 84105, Israel

(Received 26 December 2013; accepted 10 March 2014; published online 25 March 2014)

Spatially non-uniform electric fields can phase separate initially homogeneous mixtures of liquids. Here, we investigate the dynamics of phase separation using a modified Cahn-Hilliard equation and find three kinetically distinct regimes in the phase diagram: (1) discontinuous and (2) continuous interface formation kinetics and (3) a metastable state. By considering all possible solutions of the free energy density, we are able to map the time behavior in the vicinity of the interface as a series of equilibrium interfaces "moving" in the parameter space of the equilibrium phase diagram. The kinetic phase diagram, consequently, contains an "emergence line" that delineates the experimental conditions where a non-equilibrium interface can be *forbidden* from forming close to a charged surface. When the interface can form on the charged surface, an abrupt transition occurs that produces electrical signatures which distinguish the discontinuous from the continuous transition region. The third kinetic regime describes non-spontaneous phase separation and potential metastable states, and is bounded by the "electrostatic spinodal" line. The equivalent kinetic regimes exist in closed systems and can be found by considering an effective concentration in an open system. © *2014 AIP Publishing LLC*. [http://dx.doi.org/10.1063/1.4869113]

I. INTRODUCTION

The desire to control materials on the sub-micrometer scale motivates basic and applied research and has led to an abundance of works.[1–4] Due to the ease and versatility of applying electric fields, the conductivity and polarizability differences between substances have been exploited for a variety of purposes that range from steering individual molecules or objects[5,6] to creating droplet "microreactors".[7] In this spirit, a significant body of work also includes establishing electric field induced phase separation.[8–14] Research in this area typically focuses on uniform electric fields; however, fluid demixing with such fields usually requires excessively large potentials.[8–10]

By contrast, recent work with spatially nonuniform electric fields shows that phase separation can readily occur with much smaller surface charges or potentials.[15–17] The spatial non-uniformity of the field reversibly confines the two liquids to well-defined regions of physical space and *creates* an interface between them. In this "electroprewetting" transition, the more polar liquid wets the electrode.[18] The spatial dependence of the demixing means that equilibrium cannot be determined using the usual "common tangent" construction, and a different formalism is consequently required. We recently overcame this challenge by implementing local markers to successfully construct the phase diagram.[19]

In this manuscript, we extend this formalism to phase separation kinetics. Unlike standard nucleation processes and spinodal decomposition, the properties of the interface in time depend on its location in space. Interestingly, we find that the kinetic behavior can be mapped as an equilibrium interface moving in parameter space of the phase diagram. Specifically, we demonstrate that an interface can be forbidden from forming close to the electrode for certain conditions, and that this forbidden zone affects how an interface emerges in time. The "emergence line" separates these conditions in the phase diagram. On one side of this line a forbidden zone exists and the interface first appears far from the electrode and continuously in time. Conversely on the other side of this line, an interface forms abruptly on the electrode surface. Such discontinuous behavior leads to changes in the current and capacitance that can be detected experimentally. Finally, we also confirm predictions of an "electrostatic spinodal" and metastable states for diffusion limited kinetics in the absence of fluctuations. We also discuss similarities and differences in the kinetic behavior between open and closed systems.

II. THEORY

We begin with a mean-field coarse-grained description of a binary mixture composed of liquids A and B. The total free energy $\mathcal{F}$ for a volume V is the sum of mixing $\mathcal{F}_\mathrm{m}$, electrostatic $\mathcal{F}_\mathrm{e}$, and interfacial $\mathcal{F}_\mathrm{i}$ free energies to give

$$\mathcal{F} = \int_V (\mathcal{F}_\mathrm{m} + \mathcal{F}_\mathrm{e} + \mathcal{F}_\mathrm{i})\,\mathrm{d}V. \tag{1}$$

The free energy of mixing is $\mathcal{F}_\mathrm{m} = kTf_\mathrm{m}/v$, where v is molecular volume, k is Boltzmann constant, and T is temperature. The dimensionless energy density f_m should have a "double well" shape, and here we use the following Landau expansion of a regular mixing energy around the critical volume fraction ϕ_c,

$$f_\mathrm{m} \approx (2 - N\chi)(\phi - \phi_c)^2 + \frac{4}{3}(\phi - \phi_c)^4 + const., \tag{2}$$

where ϕ is the volume fraction of component A ($0 \le \phi \le 1$), and $\chi \sim 1/T$ is the Flory interaction parameter.[20] We set $\phi_c = 0.5$ and $\chi = 2T_c/T$, where T_c is the critical temperature.

The electrostatic free energy $\mathcal{F}_e = kTf_e/v$ is given by

$$\mathcal{F}_e = \pm\frac{1}{2}\varepsilon_0\varepsilon(\phi)|\nabla\psi|^2, \tag{3}$$

where ε_0 is the vacuum permittivity, and ψ is the electrostatic potential ($\mathbf{E} = -\nabla\psi$). The sign depends on the boundary conditions, where the positive (negative) sign indicates constant charge (potential). The constitutive relation $\varepsilon(\phi)$ defines a nontrivial dependence of permittivity on composition. Here we mainly consider a linear relation, $\varepsilon(\phi) = (\varepsilon_A - \varepsilon_B)\phi + \varepsilon_B$, where ε_A and ε_B are the dielectric constants for pure liquids A and B, respectively.

The interfacial free energy $\mathcal{F}_i = kTf_i/v$ includes the energetic penalty associated with composition gradients and is given by[20]

$$f_i = \frac{1}{2}\chi\lambda^2|\nabla\phi|^2, \tag{4}$$

where λ is a constant related to interface width.

In equilibrium, the fields ψ and ϕ obey the following Euler-Lagrange equations:

$$\frac{\delta\mathcal{F}}{\delta\psi} = \nabla\cdot[\varepsilon_0\varepsilon(\phi)\nabla\psi] = 0, \tag{5}$$

$$\frac{\delta\mathcal{F}}{\delta\phi} = \mathcal{F}_m' - \frac{1}{2}\varepsilon_0\varepsilon'(\phi)|\nabla\psi|^2 - \nabla\cdot\left[\frac{kT}{v}\chi\lambda^2\nabla\phi\right] - \tilde{\mu} = 0, \tag{6}$$

where the "prime" represents a derivative with respect to ϕ, and $\tilde{\mu} = kT\mu/v$ is the chemical potential. For closed systems (canonical), μ is adjusted to satisfy the mass conservation constraint, $\langle\phi\rangle = \phi_0$, where ϕ_0 is the average composition. For open systems (grand canonical) in contact with a large reservoir at composition ϕ_0, $\mu = \partial f_m(\phi_0, T)/\partial\phi$.

After an electric field is applied, the initially homogeneous liquid changes its composition until a new equilibrium (or long-time steady-state) is reached. For the dynamics we therefore use the "model B" theoretical framework[21,22] supplemented by Laplace's law to obtain

$$\frac{\partial\phi}{\partial t} = \nabla\cdot\left[D\nabla\frac{\delta\mathcal{F}}{\delta\phi}\right], \tag{7}$$

$$\nabla\cdot[\varepsilon_0\varepsilon(\phi)\nabla\psi] = 0, \tag{8}$$

where D is the diffusivity constant. Equation (7), the Cahn-Hilliard equation, is the continuity equation for the mixture composition.[23] And the boundary conditions for Eqs. (6) and (7) are

$$\nabla\frac{\delta\mathcal{F}}{\delta\phi}\cdot\mathbf{n} = 0, \tag{9}$$

$$\nabla\phi\cdot\mathbf{n} = 0, \tag{10}$$

respectively, where $\mathbf{n}$ is the unit vector normal to the wall.

To understand the fundamental dynamic behaviors, we focus on three basic shapes (cylinder, sphere, and wedge), where $\mathcal{F}$ depends only on the radial coordinate. The inner and outer boundaries for the cylindrical geometry are radii R_1 and R_2, respectively, Fig. 1(a). And, the radially symmetric profiles are one-dimensional $\phi = \phi(r)$ and $\psi = \psi(r)$, where r is the distance from the inner cylinder's center. With a constant charge density σ on R_1, we obtain $\mathbf{E}(r) = \sigma R_1^n/(\varepsilon_0\varepsilon(\phi)r^n)\hat{\mathbf{r}}$, where $n = 1$. Using a similar construction for concentric spheres, we obtain the same expression $\mathbf{E}(r)$ with $n = 2$. Combining this result with $\mathbf{E} = -\nabla\psi$ in Eq. (6), we get

$$\frac{\delta f}{\delta\phi} = f_m' - \frac{v}{2kT\varepsilon_0}\left(\frac{\sigma R_1^n}{r^n}\right)^2\frac{\varepsilon'(\phi)}{\varepsilon(\phi)^2} - \nabla\cdot[\chi\lambda^2\nabla\phi] - \mu. \tag{11}$$

The wedge geometry consists of two "misaligned" plates with an opening angle θ, Fig. 1(b). For a constant potential boundary condition, $\mathbf{E}(r) = (V/r\theta)\hat{\vartheta}$, where V is the potential difference across the electrodes, r is the distance from the imaginary intersection of the two plates, and ϑ is the azimuthal angle. Combining this result with Eq. (6), we get

$$\frac{\delta f}{\delta\phi} = f_m' - \frac{v}{2kT}\left(\frac{V}{r\theta}\right)^2\varepsilon_0\varepsilon'(\phi) - \nabla\cdot[\chi\lambda^2\nabla\phi] - \mu. \tag{12}$$

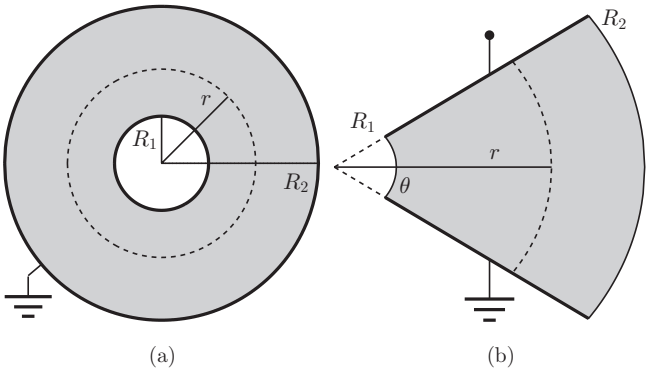

FIG. 1. Model systems. (a) Cross section through the diameter of concentric cylinders or spheres. Distance r is measured from the center of the cylinder/sphere, and the boundaries are located at R_1 and R_2. (b) Cross section of two flat-plate electrodes with an opening angle θ. Distance r is measured from the "intersection" of the two plates, and the boundaries R_1 and R_2 mark the ends of the plates. Shading shows the space occupied by the liquid mixture.

III. PHASE DIAGRAM AND FREE ENERGY

To understand the dynamics of phase separation we first highlight the important aspects of the phase diagram. The phase diagram contains three distinct equilibrium regions,[19] which we call "global demixing," "local demixing," and "mixing." Figure 2(a) shows these regions in open cylinder and open sphere geometries with a linear $\varepsilon(\phi)$, and in open wedge geometries with a quadratic $\varepsilon(\phi)$, where the second derivative $\varepsilon'' \equiv \mathrm{d}^2\varepsilon/\mathrm{d}\phi^2 = -2$. In the "global demixing" region, which is below the zero-field binodal curve [dashed line in Fig. 2(a)], phase separation can occur without an electric field. By contrast, liquid separation marked by a sharp interface cannot occur under *any* applied electric field in the "mixing" region of the phase diagram, Fig. 2(a). Instead, the electric field produces gradual changes in liquid composition. In the "local demixing" region [gray area in Fig. 2(a)], a sufficiently strong electric field can induce liquid

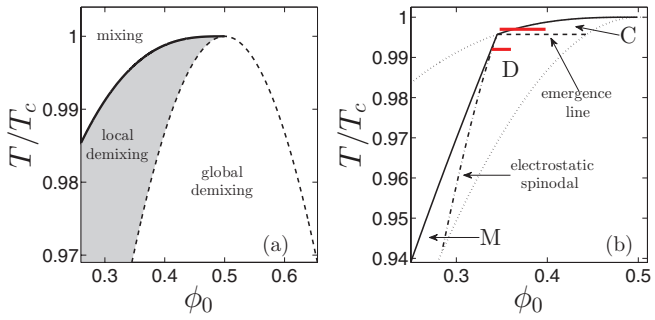

FIG. 2. Mixing-demixing phase diagram with a non-uniform electric field for open systems. (a) Phase diagram in the $\phi_0 - T$ plane showing regions where phase separation is possible without an electric field ("global demixing"), is possible with an electric field ("local demixing"), and is not possible with any electric field ("mixing"). Dashed and solid lines are the regular binodal curve and the electrostatic binodal, respectively. (b) The particular demixing zone (solid line) for $\sigma = 1 \times 10^{-3}$ C/m^2 within the local demixing region (dotted lines) showing all kinetically important features in the $\phi_0 - T$ plane. "C" and "D" denote continuous and discontinuous interface formation kinetics, while "M" denotes metastable region. The upper and lower red bars mark $\phi_{0\text{eq}}$ for data in Figs. 5(a) and 6(a), respectively (see text).

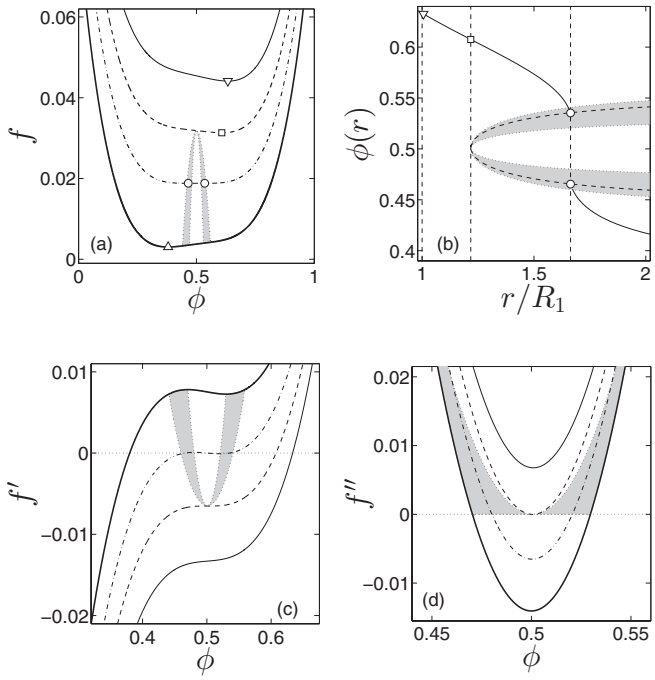

FIG. 3. Free energy density $f(\phi, r)$ for an open cylinder system. (a), (c), and (d) f, f', and f'', respectively, versus ϕ at distance $r = R_1$ (thin solid line), r_e (dashed line), r_i (dashed-dotted line), and a large value (thick solid line) for $\phi_0 = 0.38$, $T/T_c = 0.9965$, and $\sigma = 1.1 \times 10^{-3}$ C/m^2. Symbols in (a) mark minima for each curve. (b) $\phi(r)$ versus normalized distance r of the minimized solution to f in (a). Dashed vertical lines from left to right show $r = R_1$, r_e, and r_i. Shaded areas in all figures mark regions where f' is degenerate and $f'' \geq 0$. In this and in all other figures $T_c = 298$ K, $\varepsilon_A = 5$, $\varepsilon_B = 3$, $R_1 = 1\ \mu$m, and $v = 1 \times 10^{-26}$ m^3.

demixing. This region is bounded from below by the binodal curve and from above by the "electrostatic binodal" curve, solid line in Fig. 2(a).

A finite value of surface charge induces phase separation within a limited zone of the local demixing region, marked by solid lines in Fig. 2(b). In this zone, the location of the interface between the two liquids r_i can be approximated by[19]

$$\left(\frac{\sigma R_1^n}{r_i^n}\right)^2 \approx -\frac{2kT\mu\varepsilon_0\varepsilon(\phi_c)^2}{v\varepsilon'(\phi_c)} \tag{13}$$

for cylindrical and spherical geometries, and by

$$\left(\frac{V}{\theta r_i}\right)^2 \approx -\frac{2kT\mu}{v\varepsilon_0\varepsilon'(\phi_c)} \tag{14}$$

for wedge geometries. The remainder of this paper focuses on the kinetic behavior within the demixing zone.

An intuitive understanding of liquid-liquid behavior with non-uniform electric fields can be obtained by considering the free energy. For a given set of parameters (ϕ_0, T, σ, R_2, etc.), the set of all possible values of the free energy density f for a range of local composition ϕ changes as a function of position r, Fig. 3, as well as time t. In other words, the set of all possible values of f can be thought of as a "landscape" or surface that changes in space and time. Without the constraint of material conservation, the f-surface also remains constant in time in open systems, which greatly simplifies the analysis of kinetic behavior.

The curved surface in Fig. 4(a) presents a "zoomed in" view of f' as a function of ϕ and r for the same parameters as Fig. 3. The equilibrium solution resides in the intersection between the f' surface and the horizontal plane at $f' = 0$. This intersection gives the dashed curve in Fig. 4(b), while the solid line marks the particular $\phi(r)$ profile that minimizes the total free energy. The dynamic solutions, however, are not restricted to this plane, and liquid composition can rearrange in a complex manner, Fig. 4(c).

From Figs. 4(b) and 4(c) it is clear that a one-to-one correspondence between (f', r) and ϕ does not always hold. We call this non-one-to-one correspondence a "degeneracy." Since interfaces can develop when there is a degeneracy, these mathematical features play a significant role in interface dynamics (Secs. IV and V). For the special case of degenerate solutions with $f' = 0$, we will show in Sec. VI how metastable solutions emerge.

IV. THE INTERFACE AND THE EMERGENCE LINE

Previous work considered a simplified free energy f, where $\lambda \to 0$ so that $f_i \to 0$.[15–17,19] This limit typically applies to "large" systems when T is not too close to T_c. As a consequence, the continuous concentration profile $\phi(r)$ appears discontinuous on relevant length scales. We find that the inclusion of a non-zero f_i does not qualitatively change the liquid behavior for the range of λ and temperatures that we have investigated. However, the equilibrium conditions that define the appearance of an interface do not hold for dynamics.[15–17,19] Moreover, even a small but non-zero value of λ in f_i destroys the discontinuity and leads to a diffuse interface. These properties make the task of distinguishing an interface from a concentration gradient challenging.

The presence of an interface coincides with a rapid change in $\phi(r)$, Figs. 5(a) and 6(a). Figure 5(c), for example, compares $f'(r)$ versus $\phi(r)$ at a particular r, dashed line, with $\delta f/\delta\phi$ from dynamic calculations at various times,

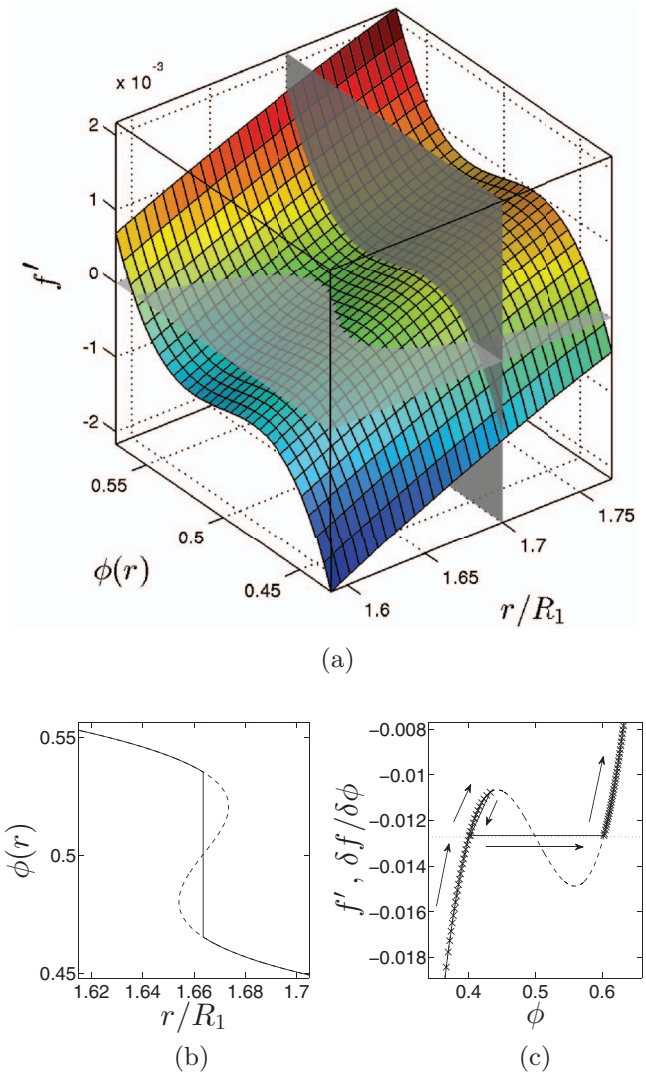

FIG. 4. The $f'(\phi, r)$ surface and dynamics. (a) f' versus ϕ and r for the same parameters as Fig. 3. Color shows the value of f'. The horizontal plane, where $f' = 0$, is shown as a dashed curve in (b). The solid line in (b) is the $\phi(r)$ profile that minimizes the total free energy. The vertical plane in (a) is a schematic for the type of view in (c), where r is constant. In (c), $\phi_0 = 0.36$, $T/T_c = 0.9824$, $\sigma = 1 \times 10^{-3}$ C/m^2, and $r/R_1 = 1.004$. Dashed line shows f', while symbols mark $\delta f/\delta\phi$ in time from the dynamic calculations. Arrows indicate the direction of change in time. Dotted line marks the location of an equilibrium interface with $\phi_{0\text{eq}} = 0.322$ (see text).

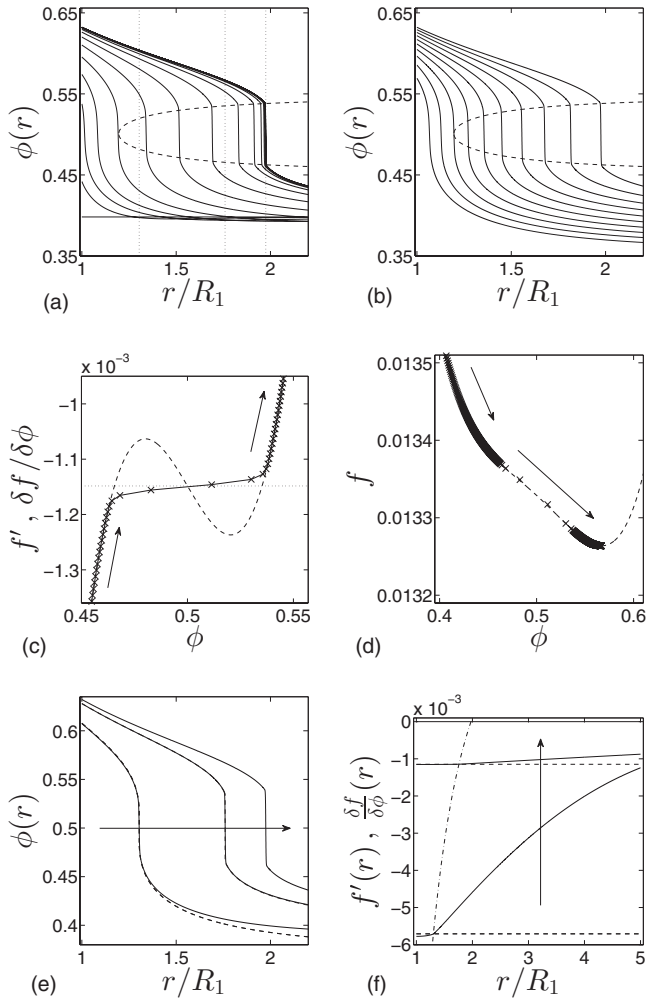

FIG. 5. Profiles from dynamic calculations. (a) $\phi(r)$ versus r showing various snapshots in time t at intervals regularly spaced on a logarithmic scale for $\phi_0 \approx 0.398$. Dashed curve shows equilibrium-like behavior of the interface. Dotted lines show location of data in (c)–(f). (b) $\phi(r)$ versus r showing steady-state solutions for $\phi_0 \approx 0.353$–0.398 in 0.005 increments (left to right). Dashed curve shows equilibrium behavior of the interface for all ϕ_0. (c) and (d) f' (or $\delta f/\delta\phi$) and f versus ϕ at $r/R_1 \approx 1.76$ [middle dotted line in (a)]. Dashed lines show f', while symbols mark $\delta f/\delta\phi$ in time from dynamic calculations. Arrows indicate the direction of change in time. Dotted line in (c) marks location of an equilibrium interface with $\phi_{0\text{eq}} \approx 0.391$. (e) and (f) ϕ and f' (or $\delta f/\delta\phi$) versus r for the interface locations marked by dotted lines in (a). Solid lines show dynamic calculations, while dashed lines show equilibrium solutions with different $\phi_{0\text{eq}}$. Arrows show the direction of time or increasing $\phi_{0\text{eq}}$. Dashed-dotted line in (f) shows the location of the equilibrium interface. In all figures, $T/T_c = 0.997$, $\sigma = 1 \times 10^{-3}$ C/m^2.

symbols, and arrows. And Fig. 5(d) displays the same data as $f(r)$ versus $\phi(r)$. The dashed line in Fig. 5(c) indicates that multiple values of ϕ yield the same value of f'. Precisely in this degenerate region, the $\phi(r)$ from dynamic calculations rapidly changes, signifying the presence of an interface at that time. Both Figs. 5(c) and 5(d) clearly show that the interface at this location is *not* part of the free energy minimum. We therefore define a dynamic interface at r as a rapidly changing $\phi(r)$ that coincides with a ϕ-degeneracy in $f'(r)$ [in particular with a vertical section of the f' surface, Fig. 4(a)].

The gray areas in Fig. 3 mark the location of all degenerate regions in $f'(r)$ that also satisfy $f''(r) > 0$ (the classical metastable region in mixtures without an electric field). These areas clearly illustrate two important kinetic phenomena: (1) an interface can be *forbidden* from forming in certain regions of physical space, and (2) interface properties (e.g., the magnitude of a discontinuity) can strongly depend on spatial location. To determine where an interface can exist we note that in Figs. 3(a) and 3(c) the degenerate region extends to infinity but can "pinch off" and terminate somewhere close to the inner electrode. For distances smaller than this termination, a one-to-one correspondence exists between (f', r) and ϕ [both vertical and horizontal sections of the f' surface, Fig. 4(a)]. The degeneracy originates from the double well in f_m, and its disappearance directly results from a spatially dependent f_e. That is, f_e can become sufficiently strong at small r's to destroy the degeneracy.

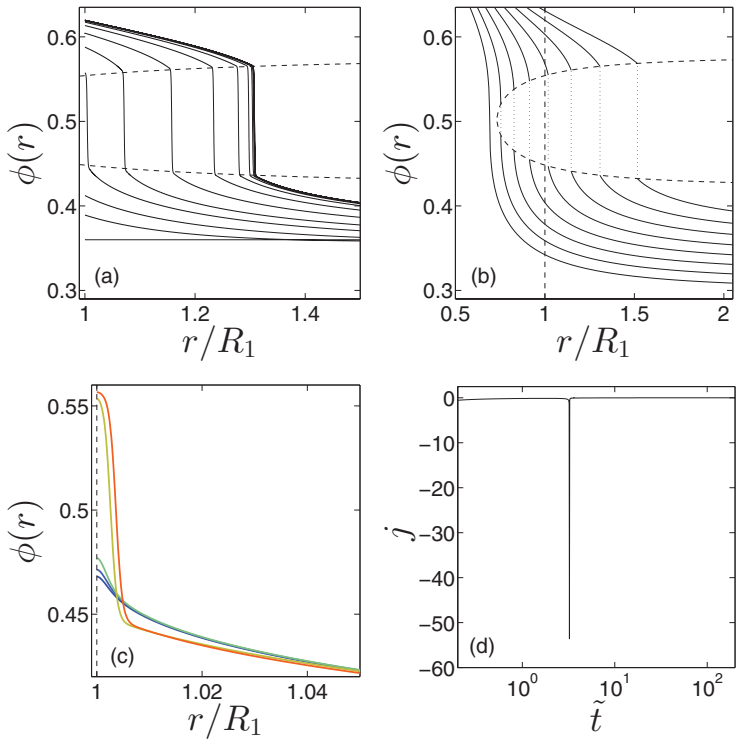

FIG. 6. Interface formation kinetics. (a) $\phi(r)$ versus normalized r showing various snapshots in time t at intervals spaced regularly on a logarithmic scale for $\phi_0 = 0.36$. Dashed lines show equilibrium-like interface behavior. The interface that appears discontinuous is smooth but rapidly varying in the numerical calculations. (b) $\phi(r)$ versus r showing *equilibrium* solutions for $\phi_0 = 0.3$–0.37 in 0.01 increments (left to right). Dashed curve shows equilibrium interface behavior for all ϕ_0. (c) $\phi(r)$ versus r for dimensionless time $\tilde{t} = DkTt/R_1^2Nv \approx 3.04$–$3.14$ in 0.024 increments (blue to red). In (a)–(c), $T/T_c = 0.992$, $\sigma = 1 \times 10^{-3}$ C/m^2. (d) Electric current density $j = \mathrm{d}\sigma/\mathrm{d}t$ (A/m^2) versus $\tilde{t}$ for similar conditions as (a), except with constant potential $V \approx 216$ V that was chosen to match the steady-state value of V in (a).

We can find the smallest distance r_e where a non-equilibrium interface can emerge by looking at the form of $f'(r)$, Figs. 3(c), 4(c), and 5(c), and noticing that $f''(r)$ also possesses negative values, Fig. 3(d). Therefore, we can search for r_e by finding where the minimum value of $f''(\phi, r_e)$ vanishes, that is, $f^{(3)}(\phi, r_e) = 0$ and $f^{(4)}(\phi, r_e) > 0$. The value of ϕ that coincides with the minimum in f'' is approximately equal to ϕ_c.[19] Beginning with $f''(\phi, r_e) = 0$ and setting $\phi \approx \phi_c = 0.5$, we obtain for cylindrical and spherical geometries

$$\left(\frac{r_e}{R_1}\right)^{2n} = -\frac{v\left(\varepsilon'\sigma\right)^2}{4k(T - T_c)\varepsilon_0\varepsilon(\phi_c)^3}, \tag{15}$$

and for wedge geometries

$$r_e^2 = \frac{v\varepsilon_0\varepsilon'' V^2}{8k(T - T_c)\theta^2}. \tag{16}$$

Mathematically, the solutions of f exist for all $r > 0$, where distances can be "real" ($R_1 \le r \le R_2$) or "virtual" [$r < R_1$, $r > R_2$, "within the electrode" or not between the plates as defined in Fig. 1(b)].[19]

The conditions where $r_e = R_1$ in Eqs. (15) and (16) hold special meaning. When $r_e < R_1$, an interface can exist everywhere in real space. Conversely when $r_e > R_1$, an interface can only exist in restricted regions of real space, namely, for any $r \ge r_e$. Setting $r_e = R_1$ in Eq. (15), we obtain the equation for the emergence line for spherical and cylindrical geometries

$$\frac{T_e}{T_c} = 1 - \frac{v(\sigma\varepsilon')^2}{4kT_c\varepsilon_0\varepsilon(\phi_c)^3}, \tag{17}$$

and with Eq. (16) for wedge geometries

$$\frac{T_e}{T_c} = 1 + \frac{v\varepsilon_0\varepsilon''}{8kT_c}\left(\frac{V}{R_1\theta}\right)^2. \tag{18}$$

Figure 2(b) shows the emergence line for the stability diagram with a cylindrical geometry.

Both Eqs. (17) and (16) resemble the equations that describe the electrostatic binodal.[19] Below, we further develop the link between kinetic and equilibrium behavior.

V. DISCONTINUOUS AND CONTINUOUS INTERFACE FORMATION KINETICS

We showed in Sec. IV where a non-equilibrium interface could exist in physical space (i.e., anywhere within the degenerate region, gray areas in Fig. 3). In this section, we discuss the specific behavior of the interface for diffusion-limited kinetics.

Since ϕ_0, which enters f through μ, disappears past the first derivative, the equations describing the kinetic properties of r_e [Eqs. (15) and (16)] and the emergence line [Eqs. (17) and (18)] do not depend on the composition in the bath. Interestingly, however, similarities in the interface exist between the time snapshots of the dynamic solution for a particular

ϕ_0, Figs. 5(a) and 6(a), and the steady-state/equilibrium solutions from varying values of ϕ_0, Figs. 5(b) and 6(b). The kinetic relaxation of the interface occurs as if an effective ϕ_0 changes in time.

The value of ϕ_0 strongly affects equilibrium $\phi(r)$ profiles by altering both the location and size of the discontinuity.[19] The solid lines in Figs. 5(b) and 6(b) show steady-state dynamic and equilibrium solutions, respectively, of $\phi(r)$ for various values of ϕ_0, while the dashed curves mark the equilibrium behavior of the interface for all ϕ_0. A change in ϕ_0 is equivalent to a change in the chemical potential. We again return to observing the time behavior of $\phi(r)$ on $f'(r)$ at a particular distance r, Fig. 5(c). Using T, σ, and setting $r_i = r$ in Eq. (13), we can obtain the $\mu_{\rm eq}$ necessary for forming an *equilibrium* interface at r. The dotted line in Fig. 5(c) indicates where the zero value of $f'(r)$ would be located with this $\mu_{\rm eq}$. Interestingly, the time-dependent solution forms an interface along this dotted line, symbols in Figs. 4(c) and 5(c).

Recalling that $\mu = f'_{\rm m}(\phi_0, T)$ for open systems in equilibrium, we can find the corresponding *equilibrium* value of $\phi_{0\rm eq}$ for $\mu_{\rm eq}$. Figure 5(e) directly compares three different profiles in time for the dynamic calculations (solid lines) with a constant $\phi_0 \approx 0.398$ versus the corresponding equilibrium solutions (dashed lines) with various $\phi_0 = \phi_{0\rm eq}$. As the differences between the dynamic and equilibrium profiles can be small, we also include $f'(r)$ and $\delta f/\delta\phi$ as a measure of how well the two profiles coincide with each other. The solid lines in Fig. 5(f) show the dynamic $\delta f/\delta\phi$ profiles, while the dashed lines indicate where the zero value of $f'(r)$ would be with each $\phi_{0\rm eq}$. It is clearly evident that in the vicinity of the interface, the dynamic $\phi(r)$ profile at a particular time and ϕ_0 behaves similar to an equilibrium $\phi(r)$ profile with a potentially *different* $\phi_{0\rm eq}$ bath.

With the previously described method for obtaining $\phi_{0\rm eq}$ [setting $r_i = r$ in Eq. (13) and using $\mu_{\rm eq} = f'_{\rm m}(\phi_{0\rm eq}, T)$], we find that each value of r yields a different value of $\phi_{0\rm eq}$. The dashed-dotted line in Fig. 5(f) shows the location of the zero value of f' with $\phi_{0\rm eq}$ as a function of r, and the corresponding range of values for $\phi_{0\rm eq}$ is marked by the upper red bar in Fig. 2(b). Similarly, the lower red bar in Fig. 2(b) shows the progression of $\phi_{0\rm eq}$ for the dynamic data in Fig. 6(a). Specifically, as the non-equilibrium interface moves from low to higher values of r with time, $\phi_{0\rm eq}$ begins at some low value and increases to ϕ_0 with time. The non-equilibrium interface therefore changes in time *as if* the ϕ_0 bath is changing in time. The dashed lines in Figs. 5(a) and 6(a) mark the equilibrium-like behavior of the interface discontinuity.

Visual inspection between Figs. 5(a) and 6(a) shows differences in how the interface emerges in time. The values of ϕ_0, T, and σ place the data in Fig. 5(a) above the emergence line ($r_e > R_1$), while those in Fig. 6(a) are located below this line ($r_e < R_1$). Consider the case where the parameters are above the emergence line ($r_e > R_1$) in the $\phi - T$ plane, Fig. 2(b). As the electric field is turned on, the more polar material accumulates first near the electrode at small values of r, Fig. 5(a). This accumulation creates a steep concentration gradient that progresses to larger values of r as time increases. When this gradient crosses r_e, an interface gradually emerges, where the "discontinuity" begins from a vanishingly small value and grows until reaching its steady-state value. We call this phenomena continuous interface formation kinetics. This behavior is the dynamic analogue to a series of equilibrium experiments with an increasing bath concentration – the bath concentration begins in the mixing region of the phase diagram and increases such that the demixing zone is entered by crossing the electrostatic binodal.

Consider the opposite case, where the experimental conditions are below the emergence line ($r_e < R_1$) in the $\phi - T$ plane, Fig. 2(b). Again, as the electric field is turned on, the high dielectric material accumulates first at small values of r, except now, the interface abruptly emerges on the surface of the electrode, Fig. 6(a). Figure 6(c) highlights how $\phi(r)$ dramatically changes the moment an interface forms. We call this phenomena discontinuous interface formation kinetics. This behavior is the dynamic analogue to a series of equilibrium experiments with an increasing bath concentration, where the demixing zone in the phase diagram is entered from the local demixing region. An experimentally more relevant quantity is the electric current. Switching to the boundary condition of constant V and matching the steady-state conditions in Fig. 6(a), we observe that the electric current density $j = {\rm d}\sigma/{\rm d}t$ rapidly changes precisely when the interface first forms, Fig. 6(d).

VI. ELECTROSTATIC SPINODAL LINE AND METASTABILITY

The left boundary of the demixing zone can in principle be found experimentally with standard electrical techniques, e.g., by measuring the current mentioned above or the electrical capacitance. Changes in ϕ_0 affect the equilibrium (or steady-state) capacitance per unit area $C = \sigma/V$ much stronger than changes in T. By using various values of T, the "baseline" behavior between ϕ_0 and C can therefore be determined, Fig. 7(a). However, for a particular value of T, colored lines in Fig. 7(a), strong deviations from this baseline behavior coincide with the appearance of a thin layer of more polar material that is separated from the bulk solution by an interface. Since both the thickness of the more polar layer [r_i in Eq. (13)] and the magnitude of the interface discontinuity decreases with increasing T,[19] the deviation from the baseline capacitance behavior as a function of ϕ_0 also decreases with increasing T, Fig. 7(a).

The results from diffusion limited dynamics, however, differ from the above description. Figure 7(a) compares steady-state (closed symbols, solid lines) with equilibrium (open symbols, dashed lines) capacitance measurements. The two measurements coincide everywhere except when (ϕ_0, T) is "just inside" the left boundary of the demixing zone. Moreover, a "jump" in the capacitance occurs as a function of ϕ_0 for various T, Figs. 7(a) and 7(b). The location of the capacitance jump in the $\phi_0 - T$ plane does not coincide with the left boundary of the demixing zone, Fig. 7(c), but instead forms another line within the demixing zone. This line, called the "electrostatic spinodal," has been previously predicted for diffusion-limited dynamics and divides spontaneous versus non-spontaneous electric field induced phase separation.[19] The predicted mechanism for this metastable behavior

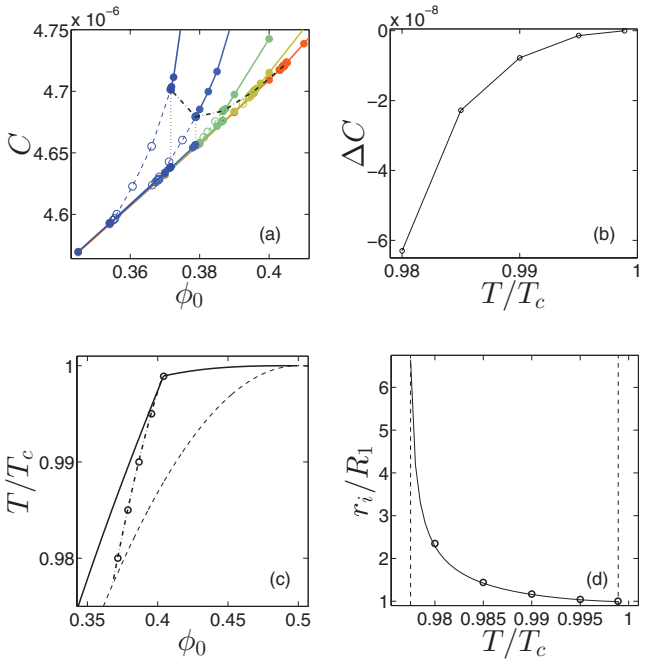

FIG. 7. (a) Steady-state capacitance $C = \sigma/V$ (F/m^2) versus ϕ_0 for equilibrium (open symbols, dashed lines) and steady-state dynamics (closed symbols, solid lines) for $T/T_c = 0.98$, 0.985, 0.99, 0.995, and 0.9989 (color blue to red) and $R_1/R_2 = 1280$. The discontinuity in C with the steady-state dynamics is highlighted by a black dashed-dotted line in (a) and plotted as ΔC versus T in (b). The location of the discontinuity in $\phi_0 - T$ plane coincides with symbols in (c). (c) Demixing zone (solid line), electrostatic spinodal (dashed-dotted line), and the binodal curve (dashed line) in the $\phi_0 - T$ plane. Symbols mark the spontaneous transition boundary for steady-state dynamic calculations. (d) The value of r_i on the electrostatic spinodal versus normalized T. Solid line is from Eq. (13), while symbols are from steady-state dynamic calculations. In all figures, $\sigma = 0.5 \times 10^{-3}$ C/m^2.

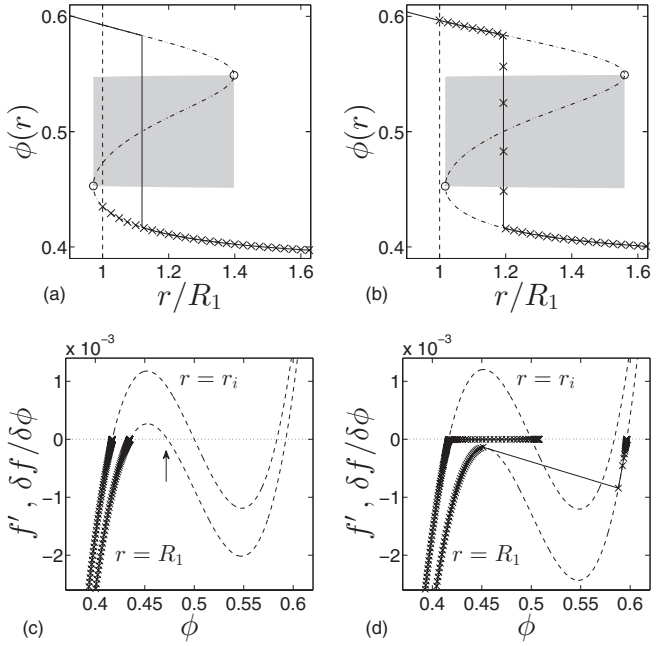

FIG. 8. Electrostatic spinodal and metastability. Profiles $\phi(r)$ versus distance r for $T/T_c = 0.99$ with $\phi_0 = 0.385$ (a) and 0.3875 (b). Dashed-dotted line shows all solutions to $f' = 0$, while solid line indicates equilibrium solution. Symbols "×" show steady-state solutions from dynamics. Symbols "◯" mark the points where $f''(\phi) = 0$ and gray rectangle is the area enclosed. (c) and (d) Same data as (a)and (b), respectively, now showing f' (or $\delta f/\delta\phi$) versus ϕ for distances $r = R_1$ and r_i. Dashed lines show f', while symbols mark $\delta f/\delta\phi$ from dynamic calculations. Arrow in (c) marks the local maximum in $f(R_1)$. In these figures, $\sigma = 0.5 \times 10^{-3}$ C/m^2.

pertained to the inflection points in $f'(r_i)$ associated with the equilibrium interface distance r_i.[19] The actual mechanism determined via dynamic calculations, Eqs. (7) and (8), does not depend on r_i and will be described in detail below. The two mechanisms yield similar results, provided that the value of r_i is close enough to R_1.

Consider the planar section in Fig. 4(a), where $f' = 0$. Two such "cuts" in the f' surface for different values of (ϕ_0, T, σ) are shown as dashed-dotted lines in Figs. 8(a) and 8(b). These combinations of $\phi(r)$ and r yield all the local extrema in f as a function of r, and the particular profile $\phi(r)$ that minimizes the total free energy is shown as solid lines. In the region resembling a rotated letter "S", $f(r)$ has a double-well shape with two minima. The maximum and minima in $f(r)$ for two distances are indirectly shown as $f'(r)$ versus ϕ in Figs. 8(c) and 8(d) [vertical sections through f' surface, Fig. 4(a)]. Correspondingly, the part of the rotated S curve located in the gray region of Figs. 8(a) and 8(b) shows the location of the local maximum, and the extent of the gray area shows where f'' is also negative.

The points labeled with "◯" symbols in Figs. 8(a) and 8(b) are given by the condition $f'(r) = f''(r) = 0$. We will focus on the location of the left-most "◯" symbol in Figs. 8(a) and 8(b) [beginning of the lower-ϕ well in $f(\phi)$], and call its location in physical space r_s. Suppose we applied an electric field to a homogeneously mixed liquid such that $r_s < R_1$, Fig. 8(a). Then an energetic barrier separates the upper- and lower-ϕ solution wells. This barrier cannot be crossed for diffusion-limited kinetics in the absence of fluctuations, and gives rise to metastable states. The "×" symbols in Fig. 8(a) show the steady-state metastable $\phi(r)$ profile from dynamics, while the "×" symbols in Fig. 8(c) show $\delta f/\delta\phi$ versus ϕ for all times with the same data. The arrow marks the local maximum at $r = R_1$.

On the other hand, suppose $r_s > R_1$. The lower-ϕ solution well does not exist for $r < r_s$, so no energetic barriers prevent access the upper-ϕ solution well. The $\phi(r)$ profile associated with the total free energy minimum is therefore accessible, and phase separation spontaneously occurs, as shown by the dynamic calculations, "×" symbols in Figs. 8(b) and 8(d).

All the combinations of (ϕ_0, T) in the stability diagram that give $r_s = R_1$ produce the "electrostatic spinodal" line, or the boundary between spontaneous transitions and metastable states. To find the electrostatic spinodal, we first hold T constant, set $r_s = R_1$, and find the value $\phi_s = \phi(r_s)$ associated with the lower-ϕ solution well by solving $f''(r_s) = 0$. We can then determine the value of ϕ_0 (via μ) that satisfies $f'(\phi_s, r_s) = 0$.

Figure 7(c) shows that the electrostatic spinodal begins at the kink in the stability diagram and travels down to intersect the binodal curve. To the "right" of this line (larger values of ϕ_0), demixing occurs spontaneously, while to the "left" (smaller values of ϕ_0) demixing occurs non-spontaneously. The electrostatic spinodal line, dashed-dotted line in Fig. 7(c), also coincides nicely with the steady-state dynamic

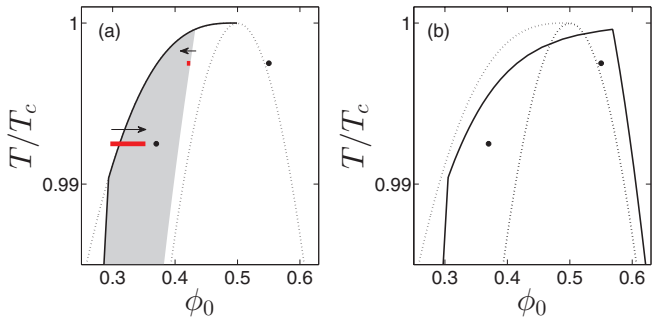

FIG. 9. Demixing zone for closed systems. The particular demixing zone (solid lines) for $\sigma = 1.5 \times 10^{-3}$ C/m^2 in (a) open and (b) closed systems with $R_2/R_1 = 5$. Dotted lines show the regular and electrostatic binodal curves. Shaded region in the open system (a) is a map of the effective ϕ_0 for the closed system demixing zone (b).[19] Black circles show the location of data in Fig. 10. Lower and upper red bars in (a) mark $\phi_{0\text{eq}}$ for data in Figs. 10(a) and 10(b), respectively, while arrows show how $\phi_{0\text{eq}}$ progresses in time.

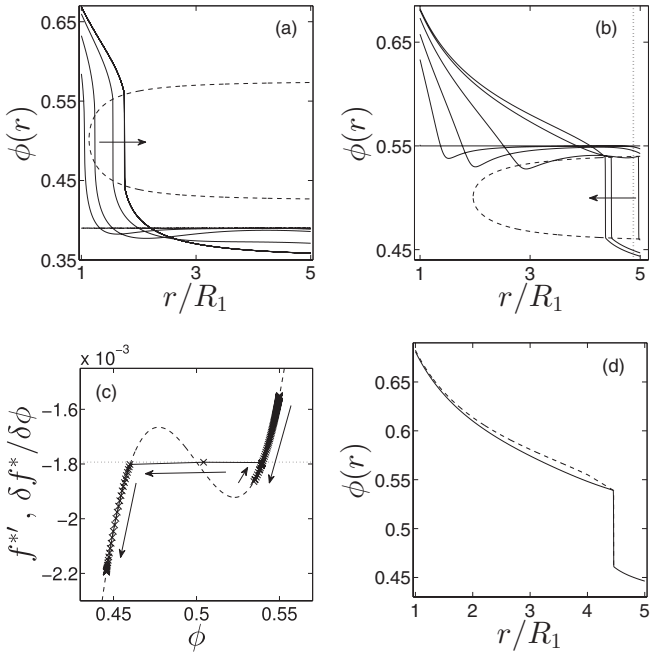

FIG. 10. Dynamic profiles for closed systems, where $R_2/R_1 = 5$ and $\sigma = 1.5 \times 10^{-3}$ C/m^2. $\phi(r)$ versus r showing various snapshots in time t at intervals regularly spaced on a logarithmic scale for (a) $\phi_0 = 0.39$, $T/T_c = 0.9925$ and (b) $\phi_0 = 0.55$, $T/T_c = 0.9975$. Dashed curves show the equilibrium-like behavior of the interface, and arrows indicate the direction of movement of the interface in time. Dotted line in (b) shows the location of data in (c). (c) $f^{*\prime}$ (or $\delta f^*/\delta\phi$) versus ϕ at $r/R_1 \approx 4.88$. Dashed lines show $f^{*\prime}$, while symbols mark $\delta f^*/\delta\phi$ from dynamic calculations. Arrows indicate the direction of change in time. Dotted line in (c) marks location of an equilibrium interface with $\phi_{0\text{eq}} \approx 0.422$. (d) $\phi(r)$ versus r for dynamic calculations (solid line) in (b) and equilibrium (dashed line) with $\phi_{0\text{eq}} \approx 0.42$.

calculations, symbols. The location of the interface r_i appears at distances greater than R_1, with $r_i = R_1$ only at the kink. Using Eq. (13) to approximate the location of r_i along the electrostatic spinodal, line in Fig. 7(d), we find an excellent agreement with steady-state dynamics (symbols).

VII. CLOSED SYSTEMS

The idea of an effective ϕ_0 has been used to map the equilibrium $\phi(r)$ profile of closed systems onto that of open systems.[19] We will now extend the language of an effective ϕ_0 to the kinetics of closed systems by using the methods developed in Secs. III–VI.

Figure 9 compares the demixing zones for a particular σ in open systems versus closed systems with $R_2/R_1 = 5$. The gray region in Fig. 9(a) marks the effective ϕ_0 that maps into the closed system demixing zone in Fig. 9(b) (see Ref. 19 for details). Unlike the demixing zone for open systems, the demixing zone for closed systems, solid line in Fig. 9(b), extends across both sides of the regular binodal curve. (For the remainder of the manuscript, we consider only the regions outside the regular binodal curve.) Kinetic differences occur when the bath concentration in the closed system is either above or below below ϕ_c. For $\phi_0 < \phi_c$, Fig. 10(a), the change in $\phi(r)$ with time is analogous to that of open systems, Fig. 5(a). However, for $\phi_0 > \phi_c$, Fig. 10(b), the more polar material accumulates near R_1 while the interface emerges first at R_2 and progresses to smaller values of r. The arrow in Fig. 10(b) illustrates how the interface moves in time, as the least polar phase separates near the electrode.

Regardless of which direction the liquid moves in time, similarities in the interface exist between the time snapshots of the dynamic solution in closed systems for a particular ϕ_0, Figs. 10(a) and 10(b), and open system equilibrium solutions from varying values of ϕ_0. The surface f' of closed systems now changes in time as a consequence of material conservation and is difficult to produce; however, the regular behavior of the interface in diffusion limited kinetics still makes analysis possible. In Secs. IV and V, we defined a non-equilibrium interface without referencing where f' vanishes; moreover, we found ϕ_{0eq} by leaving μ as a free parameter in Eq. (13). So rather than using the time dependent μ in Eq. (6), we can set μ as an arbitrary constant [here we choose the open system $\mu = f'_{\text{m}}(\phi_0, T)$] to produce an effective $\delta f^*/\delta\phi$ and $f^{*\prime}$. Figure 10(c) compares $f^{*\prime}$ versus $\phi(r)$ at a particular r, dashed line, with $\delta f^*/\delta\phi$ from dynamic calculations at various times, symbols, and arrows. The dotted line in Fig. 10(c) shows the corresponding ϕ_{0eq}. Similar to the kinetics in open systems, the time dependent solution in a closed system forms an interface along this line, symbols in Fig. 10(c). The entire $\phi(r)$ profiles, Fig. 10(d), reveal the similarity in the vicinity of the interface between the closed system dynamic calculations with a constant $\phi_0 \approx 0.55$ (solid line) and the corresponding open system equilibrium solution (dashed lines) with $\phi_0 = \phi_{0eq} \approx 0.42$. The non-equilibrium interface in a closed system therefore behaves similar to an interface in equilibrium in an open system, and the dashed curves in Figs. 10(a) and 10(b) mark the equilibrium-like behavior of the interface discontinuity. We plot how ϕ_{0eq} changes in time in Figs. 10(a) and 10(b) as lower and upper red bars, respectively, with associated arrows in Fig. 9(a).

The same basic kinetic regions (continuous, discontinuous, and metastable) of the demixing zone also occur in closed systems, with some differences that pertain to the existence of a second boundary R_2. The equation for finding the emergence line is the same for open and closed systems, and this line divides the continuous and discontinuous

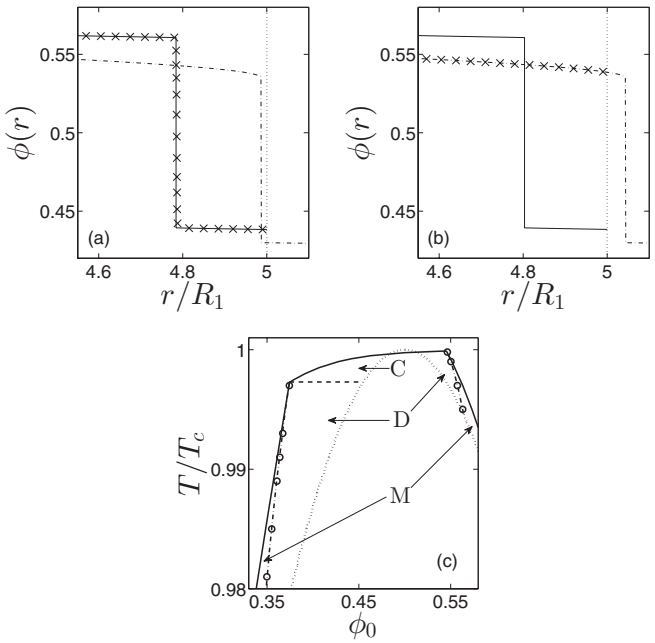

FIG. 11. Electrostatic spinodal and metastability in closed systems, where $R_2/R_1 = 5$ and $\sigma = 0.8 \times 10^{-3}$ C/m^2. Profiles $\phi(r)$ versus distance r for $T/T_c = 0.995$ with $\phi_0 = 0.5625$ (a) and 0.5635 (b). Dashed-dotted lines show the metastable solutions, while solid lines indicate the equilibrium solutions. Symbols "×" show steady-state solutions from dynamics. (c) Demixing zone (solid line), emergence line (dashed line), electrostatic spinodal (dashed-dotted lines), and the binodal curve (dotted line) in the $\phi_0 - T$ plane. Symbols mark the transition boundary for steady-state calculations. "C" and "D" denote continuous and discontinuous interface formation kinetics, while "M" denotes metastable region.

interface formation kinetic regions when $\phi_0 < \phi_c$. However, for $\phi_0 > \phi_c$, the continuous transition region does not exist as a consequence of the following: the equilibrium-like interface "opens" in the direction of R_2, dashed curves in Fig. 10(b), while the interface first emerges from R_2 and moves in the opposite direction (smaller values of r), arrow in Fig. 10(b).

The metastable region occurs on both sides of ϕ_c, Fig. 11(c). For $\phi_0 < \phi_c$, the spinodal line is found using analogous methods as an open system. However for $\phi_0 > \phi_c$, R_2 is now the relevant physical boundary, $r_s = R_2$ divides spontaneous transitions from metastable states, and the metastable states lie along the upper-ϕ solution well. Figures 11(a) and 11(b) show the $\phi(r)$ profiles for $r_s < R_2$ and $r_s > R_2$, respectively, for the equilibrium solution (solid line), metastable state (dashed-dotted line), and dynamic calculations (symbols). Due to material conservation, the upper- and lower-ϕ solution wells for closed systems, Figs. 11(a) and 11(b), are different from open systems, Figs. 8(a) and 8(b).

VIII. CONCLUSION

Non-uniform electric fields significantly alter the kinetics of liquid-liquid demixing, and in this manuscript we demonstrate how the free energy can be used to predict non-equilibrium interface behavior. The properties of the time-dependent interface depend on where the interface is located in space, in addition to bulk parameters, such as the composition of the reservoir and temperature. These location-dependent changes in the interface that occur during diffusion-limited kinetics can be approximated as a series of equilibrium interfaces with varying reservoir compositions.

Future work still remains. With the release of the radial symmetry constraint, significant patterns could emerge. For example, partial wetting with cap-like domains is predicted to occur in colloids when theories include salt in polar liquid mixtures with preferential surface adsorption.[24] This case highlights the strong influence of the local environment on the resulting wetting layer. In the much simpler theory presented in this manuscript, the possible cause for non-radial patterns is the energetic penalty that exists when dielectric interfaces are perpendicular to the field.[18] This penalty would compete with the energetic penalty of placing the less polar material in the low-field region. We predict that such an interfacial instability will develop for certain values of the field, mixture composition, and geometry.

Finally, and related to the above point, the azimuthal symmetry led to diffusive kinetics; however, better models are required when this symmetry is broken.[22] Rather than just a single interface moving outward, rapid fluid movement could create additional interfaces that lead to droplet formation and coarsening dynamics. Viscosity-related effects could compete against electric field, and on the other hand, inertial effects could help to overcome the barriers that prevent phase separation in the metastable region of the phase diagram.

ACKNOWLEDGMENTS

This work was supported by the Israel Science Foundation under Grant No. 11/10, the COST European program MP1106 "Smart and green interfaces – from single bubbles and drops to industrial, environmental and biomedical applications," and the European Research Council "Starting Grant" No. 259205.

APPENDIX: SPECIAL CASE FOR WEDGE GEOMETRIES

Differencesfrom the above discussion concerning the emergence line can occur in wedge geometries when $\varepsilon'' > 0$. Figure 12(a) shows that the degenerate region of the $\phi(r)$

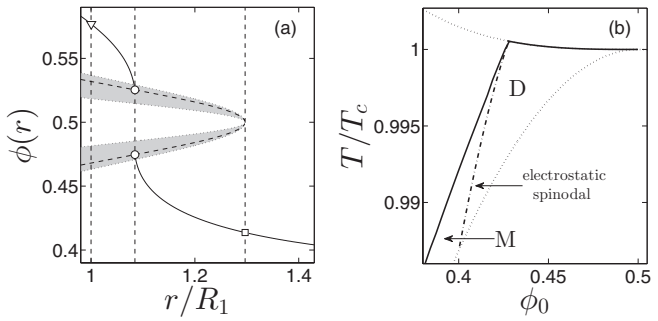

FIG. 12. Interface properties for open wedge geometries with $\varepsilon'' = 2$. (a) $\phi(r)$ versus normalized distance r for $\phi_0 = 0.375$, $T/Tc = 1.002$, and $V/\theta = 2.5$ V. Dashed vertical lines from left to right show $r = R_1$, r_i, and r_e. Shaded areas mark regions where f' is degenerate and $f'' \geq 0$. (b) Stability diagram (solid line) within the local demixing region (dotted lines) showing all kinetically important features in the $\phi_0 - T$ plane for $V/\theta = 1$ V. "D" denotes discontinuous interface formation kinetics, while "M" denotes metastable region.

profile for the wedge with $\varepsilon'' = 2$ "opens" in the reverse direction when compared with Fig. 3(b). In these cases, the interface can exist anywhere in real space for $T/T_c < 1$, and only in restricted regions of real space for $T/T_c > 1$. But since r_e is now the *largest* distance where the interface can emerge, there is no change in kinetic behavior above versus below $T/T_c = 1$ for the diffusion-limited dynamics discussed here.

[1]F. Li, D. P. Josephson, and A. Stein, Angew. Chem. Int. Edit. **50**, 360 (2011).
[2]H. Song, D. L. Chen, and R. F. Ismagilov, Angew. Chem. Int. Edit. **45**, 7336 (2006).
[3]Y. Song, J. Hormes, and C. S. S. R. Kumar, Small **4**, 698 (2008).
[4]X. Fan and I. M. White, Nat. Photonics **5**, 591 (2011).
[5]C. Asbury and G. van den Engh, Biophys. J. **74**, 1024 (1998).
[6]F. Becker, X. Wang, Y. Huang, R. Pethig, J. Vykoukal, and P. Gascoyne, P. Natl. Acad. Sci. U.S.A. **92**, 860 (1995).
[7]R. Ahmed and T. B. Jones, J. Micromech. Microeng. **17**, 1052 (2007).
[8]L. D. Landau and E. M. Lifshitz, *Elektrodinamika Sploshnykh Sred* (Nauka, Moscow, 1957), Chap. II, Section 18, Problem 1.
[9]P. Debye and K. Kleboth, J. Chem. Phys. **42**, 3155 (1965).
[10]A. Onuki, Europhys. Lett. **29**, 611 (1995).
[11]D. Beaglehole, J. Chem. Phys. **74**, 5251 (1981).
[12]K. Orzechowski, Chem. Phys. **240**, 275 (1999).
[13]M. Early, J. Chem. Phys. **96**, 641 (1992).
[14]D. Wirtz and G. Fuller, Phys. Rev. Lett. **71**, 2236 (1993).
[15]Y. Tsori, F. Tournilhac, and L. Leibler, Nature (London) **430**, 544 (2004).
[16]G. Marcus, S. Samin, and Y. Tsori, J. Chem. Phys. **129**, 061101 (2008).
[17]S. Samin and Y. Tsori, J. Chem. Phys. **131**, 194102 (2009).
[18]Y. Tsori, Rev. Mod. Phys. **81**, 1471 (2009).
[19]J. Galanis and Y. Tsori, Phys. Rev. E **88**, 012304 (2013).
[20]S. Safran, *Statistical Thermodynamics of Surfaces, Interfaces, and Membranes* (Westview Press, New York, 1994).
[21]P. C. Hohenberg and B. I. Halperin, Rev. Mod. Phys. **49**, 435 (1977).
[22]A. Bray, Adv. Phys. **51**, 481 (2002).
[23]J. W. Cahn and J. E. Hilliard, J. Chem. Phys. **28**, 258 (1958).
[24]R. Okamoto and A. Onuki, Phys. Rev. E **84**, 051401 (2011).